ADVANCED HEALTHCARE MATERIALS

www.advhealthmat.de

Disposable *Morpho menelaus* Based Flexible Microfluidic and Electronic Sensor for the Diagnosis of Neurodegenerative Disease

*Zhenzhu He, Abdelrahman Elbaz, Bingbing Gao, Junning Zhang, Enben Su, and Zhongze Gu**

Rapid early disease prevention or precise diagnosis is almost impossible in low-resource settings. Natural ordered structures in nature have great potential for the development of ultrasensitive biosensors. Here, motivated by the unique structures and extraordinary functionalities of ordered structures in nature, a biosensor based on butterfly wings is presented. In this study, a flexible *Morpho menelaus* (*M. menelaus*) based wearable sensor is integrated with a microfluidic system and electronic networks to facilitate the diagnosis of neurodegenerative disease (ND). In the microfluidic section, the structural characteristics of the *M. menelaus* wings up layer are combined with SiO_2 nanoparticles to form a heterostructure. The fluorescent enhancement property of the heterostructure is used to increase the fluorescent intensity for multiplex detection of two proteins: IgG and AD7c-NTP. For the electronic section, conductive ink is blade-coated on the under layer of wings for measuring resistance change rate to obtain the frequency of static tremors of ND patients. The disposable *M. menelaus* based flexible microfluidic and electronic sensor enables biochemical–physiological hybrid monitoring of ND. The sensor is also amenable to a variety of applications, such as comprehensive personal healthcare and human-machine interaction.

Recently, rapid diagnostic analysis, which is called point-of-care testing (POCT), has become a popular trend.[1,2] A POCT diagnostic system can provide rapid in vitro diagnostic results for untrained personnel at the patient's bedside, as well as in operating rooms, outpatient clinics, and at accident sites.[2–4] The key technical challenge of this technology to be addressed is to achieve more clinical diagnosis with less sample consumption. Meanwhile, obtaining accurate diagnoses for POCT is challenging in low-resource settings. Microfluidic analytical systems have the advantages of high integration, miniaturization, and rapid responsiveness, which represent the most promising technology for satisfying the needs of POCT.[1,3] The most common substrate materials for microfluidic chips mainly include paper, plastics, and silicon.[5] However, the high surface roughness of paper limits the resolution of the chips.[6] The high processing costs of plastics and silicon make them impractical for use in regions with resource-limited settings.[5] The disordered structures of all these materials lead to nonuniform and unmanageable liquid flows.[6] Thus, simple and easy-to-use natural ordered structures have great potential for the construction of highly sensitive and rapidly responsive detection devices, which can be applied in resource-limited areas.

Ordered microstructures with characteristic structural orientations and distinct optical and mechanical properties have become a focus of materials science research.[7,8] Ordered micro/nanostructures can be classified into two types depending on their sources, where natural ordered structures include insect wings, bird feathers, leaf epidermis, shells, and claws,[9] and artificial ordered structures include colloidal crystals, copolymers, and nanometal materials.[9–11] These ordered structures have achieved numerous applications, such as in biochemical detection, optical sensors, energy storage, and tissue engineering.[9,12] In particular, the typical natural structure of the *Morpho menelaus* (*M. menelaus*) wing has many applications because of the luminous iridescent colors produced when incident light interacts with periodic anisotropic nanostructures on the wing scales.[13–15] In recent decades, various applications have been inspired by the *Morpho* butterfly wings owing to its unique structural and optical properties, e.g., in gas sensors, infrared sensors, and surface-enhanced Raman spectroscopy substrates.[16,17]

Neurodegenerative disease (ND) is an umbrella term for chronic and progressive diseases that involves neurons, including the loss and death of neurons, which typically includes Alzheimer's disease (AD) and Parkinson's disease (PD).[18–21] The irreversible progress of ND has made it one of the main diseases that significantly affect the health of the

Dr. Z. Z. He, Dr. A. Elbaz, Dr. B. B. Gao, Dr. J. N. Zhang, Prof. Z. Z. Gu
State Key Laboratory of Bioelectronics
School of Biological Science and Medical Engineering
Southeast University
Nanjing 210096, China
E-mail: gu@seu.edu.cn
Dr. E. B. Su
Getein Biotech
Inc. No.9 Bofu Road, Luhe Distric
Nanjing 211505, Jiangsu, China

The ORCID identification number(s) for the author(s) of this article can be found under https://doi.org/10.1002/adhm.201701306.

DOI: 10.1002/adhm.201701306

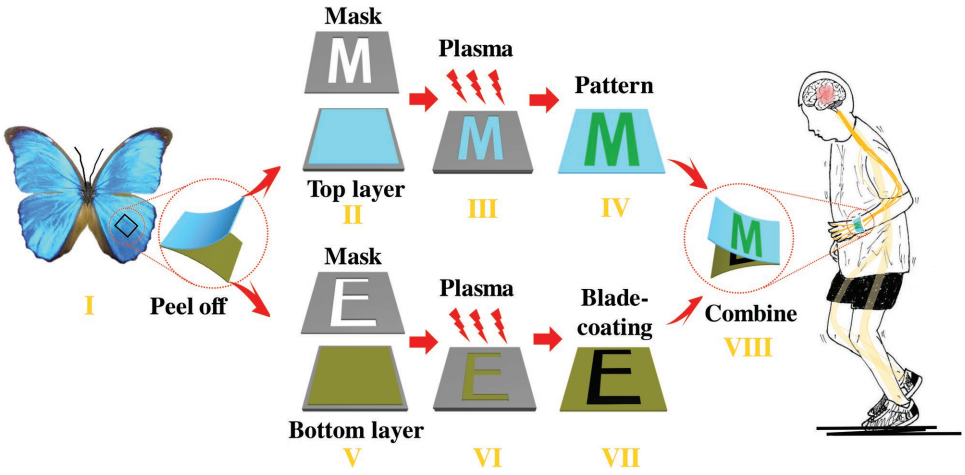

Figure 1. Schematic diagram illustrating the fabrication of *M. menelaus*-based wearable sensors. (I) The posterior wing of *M. menelaus* was used and the bright blue up layer was separated from the brown under layer. (II) The patterning mask was aligned on the up layer for plasma treatment (III) to form a patterned wing (IV). (V) Similarly, the patterned under layer was formed after plasma treatment (VI) and blade-coating with conductive ink. (VIII) The patterned wing (IV) and under layer (VII) were combined for diagnosis ("M" represents "microfluidics" and "E" denotes "flexible electronics").

elderly.[22–24] In addition, NDs have complex causes and, presently, no cure. Thus, early diagnosis and treatment are critical for facilitating timely intervention to effectively delay the progress of NDs.[25,26] At present, the diagnosis of NDs is mainly based on the detection of biochemical markers,[27] behavioral surveillance,[23] and other methods.[28] However, these methods are complex and inefficient with an unsatisfactory recognition rate.[26,27] Methods that combine multiple biochemical analyses and sensitive inspections of movement have rarely been reported. Thus, in order to improve the diagnosis and treatment of NDs, it is highly desirable to develop an innovative, rapid, and effective detection method that employs biochemical analyses and physical inspections.

In this study, we exploited the advantages of the excellent structural properties of the wings in *M. menelaus* to fabricate wearable sensors for NDs diagnosis. We selected one specimen of the posterior wing from *M. menelaus* for the early diagnosis of AD and PD. Interestingly, when we peeled off the bright blue up layer from the brown under layer, the under layer also had a striped ordered structure. Hence, the bright blue up layer comprising a hierarchical scaly micro/nanostructure with aligned microgrooves was utilized to fabricate microfluidic chips. First, an immunoassay was used to detect human immunoglobulin G (IgG) in order to verify the possibility of fluorescence enhancement using the ordered up layer of the wing. Next, a biomarker used for the early clinical diagnosis of Alzheimer-associated neuronal thread protein (AD7c-NTP) was detected quantitatively.[29,30] The brown under layer was used to achieve more flexible electronic sensing because of its striped ordered structure. After blade-coating with conductive ink, the relative resistance of the under layer changed dramatically with different bending directions and the degree of bending by the sensor. Given these desirable characteristics, this method can be used for the preliminarily diagnosis of the frequency of static tremors in PD patients.[31] In brief, we designed a wearable sensor based on the wing of *M. menelaus* for the preliminary identification of NDs. In addition, butterflies are widely distributed in nature that are readily available, and our flexible sensor can be fabricated on a large scale by utilizing high-throughput patterned masks. It is calculated that one piece of *M. menelaus* butterfly wing (≈20 cm^2) is less than \$1.2 (even available in the field where resources are limited), which can produce ≈30 microfluidic chips (0.5 cm^2) in our approach, at a cost of <\$0.04 U.S. each. Thus, we believe that the biosourced substrate will have large application prospect in biosensors.

The procedure employed for fabricating the *M. menelaus* based sensor is shown in **Figure 1**. The posterior wing section of *M. menelaus* was selected (Figure 1-I), and the bright-blue up layer (Figure 1-II) was separated from the brown under layer (Figure 1-V). To obtain the microfluidic chip, an "M"-shaped patterning mask, was aligned on the up layer for plasma treatment (Figure 1-III) to form a patterned wing (Figure 1-IV). To obtain the flexible electronic sensor, the patterned under layer was formed after plasma treatment (Figure 1-VI) and blade-coating with conductive ink (Figure 1-VII). Finally, the up layer and under layer of wings were integrated as one sensor (Figure 1-VIII), which can be attached on fingers or wrists for motion monitoring and followed with fingertip dipping in body fluid (or fluid drop on sensor) for biomarker detection.

In order to measure the resolution of the microfluidic channels, we manufactured four channels with different widths of 0.25, 0.5, 1, and 2 mm to obtain a multichannel pattern on the wings to observe the liquid flow and wetting (**Figure 2**a). Furthermore, it was possible to perform multichannel and microarray analysis on the *Morpho* wing. The infrared reflection spectra were measured precisely from the original, plasma-treated, and water-infiltrated wings (Figure 2b). We observed that the reflection peaks from the wing exhibited a slightly blue shift after plasma treatment, which might have been due to minor changes in the wing's microstructure. By contrast, after water infiltration, the reflection peaks exhibited a red shift because the water droplets filled the structure gaps in the squama structure, thus the incident light changed after interacting with the periodic nanostructures on the wing scales. The hydrophobic and hydrophilic performances of untreated and plasma treated wings were presented in Figure 2b,

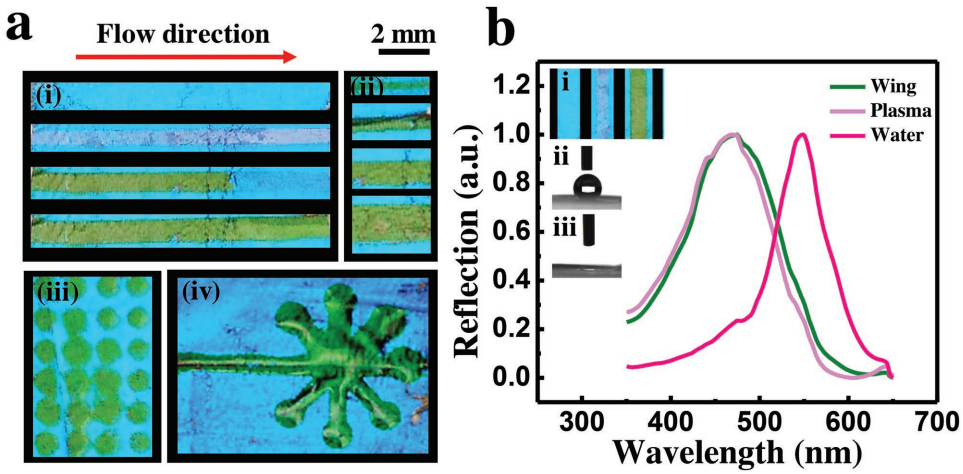

Figure 2. a) Photographs of a 1 mm channel in four states: untreated, plasma treated, water flowing, and water wicked (i); channels with different resolutions: 0.25, 0.5, 1, and 2 mm (ii); the dot array (iii), and multichannel patterns on the wings (iv). b) Reflection spectra obtained from the original, plasma-treated, and water-infiltrated wings, the insets are 1 mm channels in three states (i), contact angles (CA) of water on untreated wing (ii), and plasma treated wing (iii). (Scale bar: 2 mm).

exhibiting that the good hydrophilicity was obtained of the hydrophobic wing after plasma treatment. For the flow rate measurement section, the flow velocities of water in four different directions were contrasted, as indicated in **Figure 3**a. The 0.5 mm channels were selected to measure the flow rates parallel (Figure 3b) and perpendicular to the main vein of the wing (Figure 3c). Since the hydrophilicity is unstable after plasma treatment, the channels were further treated with dopamine (DA) to obtain the permanent hydrophilicity. The results revealed that the velocities were anisotropic owing to the orientation arrangement of the scale structure on wings, the flow velocity along the downward path of the vein is faster than the reverse direction, and the velocity of the DA treated channel is faster than the untreated in the horizontal direction. As for the vertical directions, the difference of flow velocities was not as obvious in different directions and for different treatments. Consequently, the appropriate reaction time can be determined as required, and we designed and fabricated

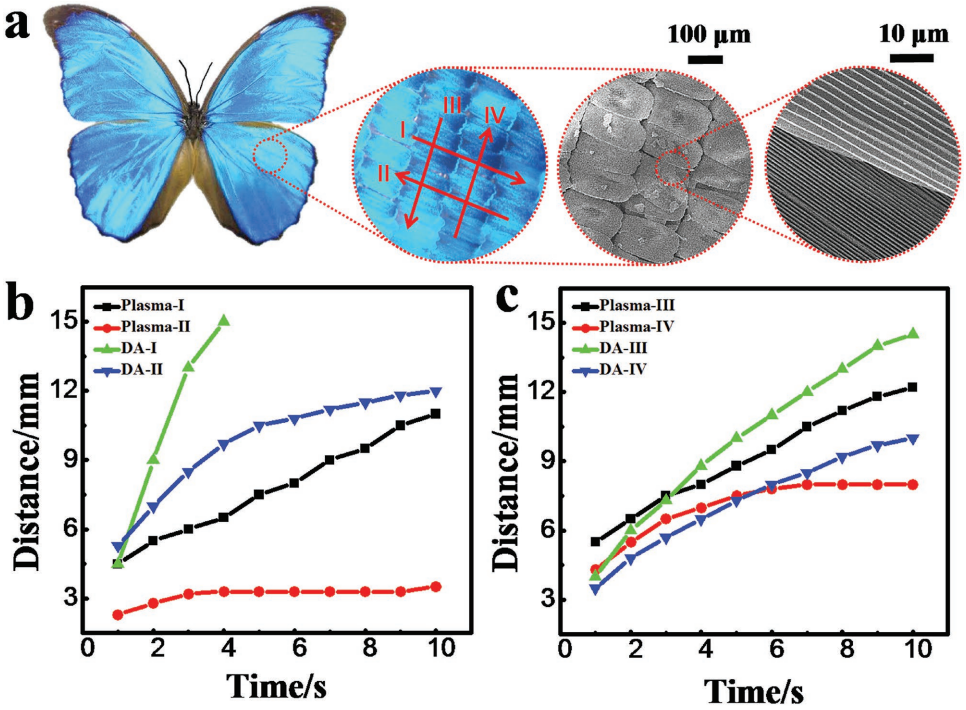

Figure 3. The microstructure and anisotropic wetting character of the wing. a) A photograph of *M. menelaus*, a magnification optical image (I, II, III, and IV represent different directions of water flow as indicated by the arrows), an SEM image on the same scale (scale bar: 100 μm), and a magnification SEM image (scale bar: 10 μm) (left to right). b) The flow conditions of a 0.5 mm channel parallel to the main vein treated by plasma and DA. c) The flow conditions of a 0.5 mm channel perpendicular to the main vein treated by plasma and DA.

microfluidic channels parallel to the main vein of the wing in followed experiments.

Previous studies have shown that strong fluorescence enhancement is obtained with photonic crystals (PhCs).[32,33] PhCs can either enhance or inhibit fluorescence emission depending on the relative position of the fluorescence emission wavelength and the stopband of the PhCs.[32] The *Morpho* butterfly wing also has a bright color and periodic structure, so it was utilized to enhance the fluorescence of fluorochrome to improve the detection sensitivity. To verify this enhancement, 0.2 µL aliquots of phosphate buffered saline (PBS) (pH = 7.4) containing fluorescein isothiocyanate (FITC)-labeled human IgG or sulfo-cyanine3 NHS ester (Cy3)-labeled human IgG were dropped separately onto a glass substrate and the treated wings (**Figure 4**a). The fluorescence intensity of FITC was higher on the glass than on the wings, and the background signal was large. By contrast, the fluorescence intensity of Cy3 was clearly enhanced on the wing with a relatively low background level. The fluorescence spectra of *M. menelaus*, FITC, and Cy3 were then determined to understand this phenomenon (Figure S1, Supporting Information). As shown in Figure S1 (Supporting Information), the *M. menelaus* wing had two emission peaks at 550 and 665 nm when excited at 445 nm, while FITC had an emission peak at 530 nm when excited at 488 nm, and Cy3 had its maximum emission peak at 570 nm when excited and 550 nm. Hence, there was an overlap between the emission spectra of FITC when excited at 488 and the 550 nm emission peak of *M. menelaus*, which resulted in a high background signal. By contrast, the emission peak of Cy3 was far from the emission area of *M. menelaus*, which had a relatively low intensity at 570 nm.

In order to obtain more intense signals, we combined SiO_2 nanoparticles and the *M. menelaus* wing to form a heterostructure.[34,35] We compared three types of SiO_2 nanoparticles with diameters of 243, 265, and 331 nm, which exhibited different photonic bandgaps of 550, 600, and 750 nm, where the 600 nm SiO_2 nanoparticles were confirmed as the best choice (Figure 4b). This is because the 600 nm photonic bandgap partially overlapped with the emission spectrum of Cy3 (Figure S1, Supporting Information) and matched the leaky eigenmodes of the PhCs with an adequate emission wavelength to achieve enhanced light emission. Next, we dropped an aqueous suspension of monodisperse SiO_2 nanoparticles onto the wing surface to form a heterostructure (Figure 4b) and the fluorescence intensity of Cy3 on the heterostructure was more than double that of the wing. We then optimized the concentration of SiO_2 nanoparticles and measured the corresponding reflectance spectra (Figure S2, Supporting Information). We discovered that a peak from *M. menelaus* was only produced without the SiO_2 nanoparticles, whereas there were two peaks as the concentration increased and a single peak with SiO_2 when the concentration increased to 20% (w/v). Thus, the intensity of both the *M. menelaus* peaks and the SiO_2 nanoparticles were relatively high with 10% (w/v) SiO_2 nanoparticles, suggesting that this combination was optimal for enhancing the fluorescence of Cy3. Scanning electron microscopy (SEM) images also verified this finding because the SiO_2 nanoparticles only filled the strip spaced between the scales with 10% (w/v) SiO_2 nanoparticles, whereas the strip disappeared when the concentration increased to 20% (w/v) (Figure S2, Supporting Information).

To obtain a flexible electronic sensor, we utilized the under layer of the wing with an ordered structure. However, it was nonconductive, so conductive ink was blade-coated on the surface after the plasma treatment to obtain a conductive surface (**Figure 5**a). The electrical characteristics of the electronic sensor are illustrated in Figure 5. Large changes in the relative resistance with the bending direction of the sensor occurred when the bending direction coincided with the direction of the strips on the under layer. Therefore, the relative resistance exhibited more significant changes compared with that perpendicular to the direction of the strips (Figure 5b). As a result, the electronic sensor exhibited enhanced sensitivity when the bending direction was in the same direction as the strips compared with that

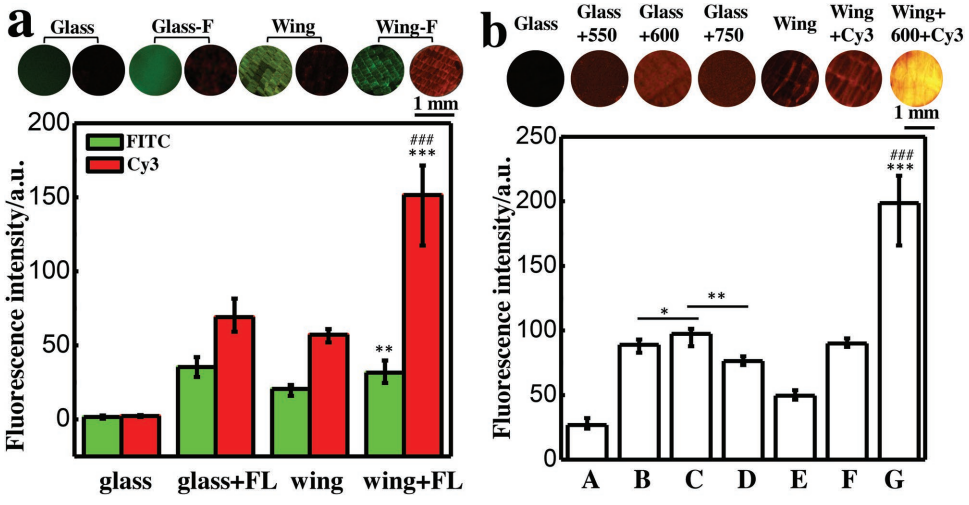

Figure 4. a) Fluorescence intensity obtained when 0.2 µL aliquots of 100 µg mL^{-1} FITC-labeled or Cy3-labeled human IgG were dropped onto a glass substrate and the treated *Morpho* wings (scale bar: 1 mm). b) Fluorescence intensity measured with different sizes of SiO_2 nanoparticles and wings with 0.2 µL aliquots of 100 µg mL^{-1} Cy3-labeled human IgG. A: Glass, B: glass + 550, C: glass + 600, D: glass + 750, E: wing, F: wing + Cy3, and G: wing + 600 + Cy3. The level of significance was set as $^{*}p < 0.05$, $^{**}p < 0.01$, and $^{***}p < 0.001$ compared to samples on glass; $^{###}p < 0.001$ compared to samples on the wings. (Scale bar: 1 mm).

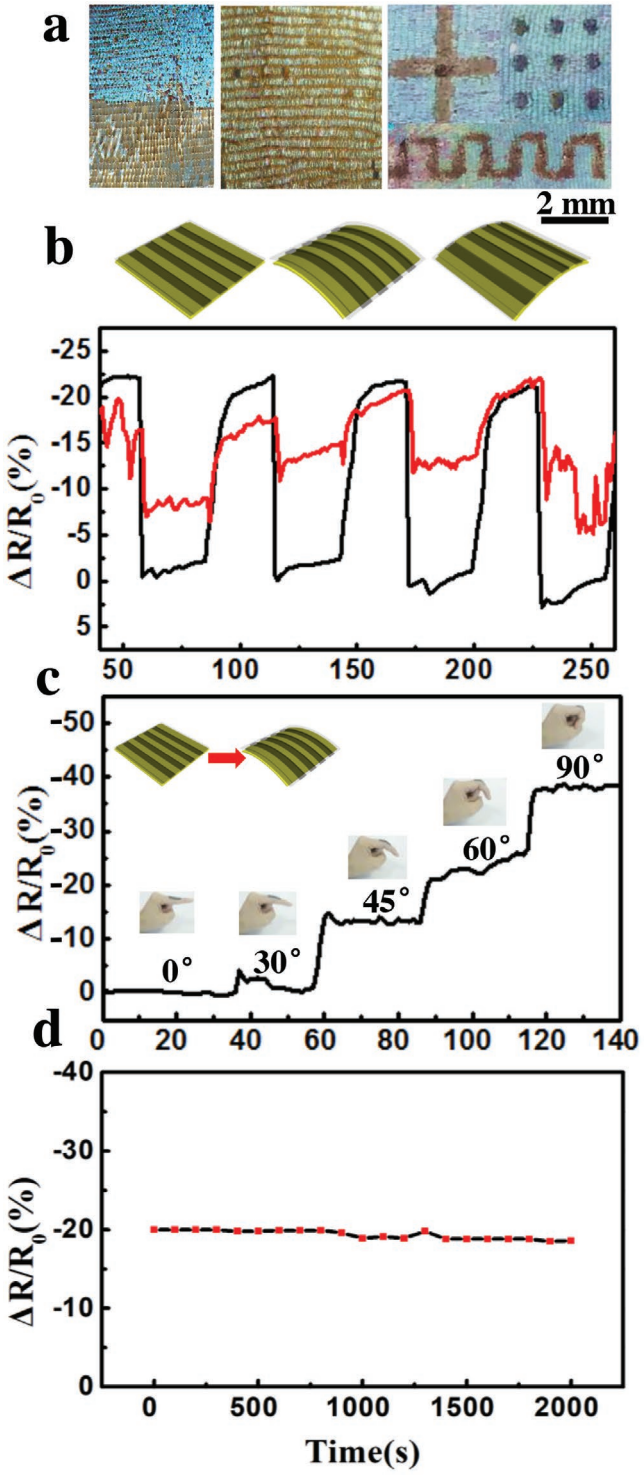

Figure 5. Electromechanical properties of the flexible sensor fabricated using the under layer of the wing. a) Optical images of the under layer: half of the peeled off up layer (left), under layer (middle), and patterned under layer (right). b) Relative changes in resistance with different sensor bending directions. The black line represents the second flexuosity and the red line is the third flexuosity, as shown in the upper row. c) Relative changes in resistance with finger bending in different angles, the inset indicates the bending direction. d) The mechanical stability test with wrist bending at a frequency of 0.2 Hz for 2000 s. (Scale bar: 2 mm).

when perpendicular to the direction of the strips. The structure of the under layer of the wing had similar scale characteristics, so the ordered direction of the scales was perpendicular to the direction of strips, as shown in Figure 5a, and the adjacent scales overlapped in a consistent direction, but the scales perpendicular to the direction of the strips were quite widely separated. Figure S3 (Supporting Information) exhibited the SEM images of the original under layer of the wing and the under layer of the wing after blade-coating with conductive ink under different magnification, where the aligned microgrooves on the scales were filled with the conductive ink, and the wing kept scales structure at the micrometer level. Consequently, when the bending direction agreed with the direction of the strips, the distance between the adjacent scales increased, thereby causing a substantial relative change in resistance, whereas there was only a small change in the vertical direction. As a result, we utilized a consistent direction in the subsequent trials. Figure 5c illustrates the detection of finger bending, which coincided with the direction of the strips, thereby obtaining various responses at different angles. In addition, the mechanical stability test is shown in Figure 5d, the sensor exhibited consistent responses even under >400 cycles with wrist bending at a frequency of 0.2 Hz for 2000 s.

For the integrated wearable sensor, the microfluidic chip made by the up layer of *M. menelaus* was integrated with the flexible electronic sensor with double-sided tape, to conduct physiological and biochemical signal sensing (**Figure 6**a). For the microfluidic system, we fabricated a multichannel chip for detecting the fluorescence of human IgG and AD7c-NTP in a fluorescence immunoassay. As is shown in Figure 6b, a specimen of the wing was treated with plasma to form hydrophilic channels, where region A is the inlet of the sample, region B/D are preloaded with fluorescence-labeled antibodies (i.e., FITC and Cy3), region C/E are the detection reservoirs preloaded with the capture antibody, and the outlet is depicted as a square waste reservoir. For the detection of AD7c-NTP with Cy3-labeled antibody, a 0.2 µL aliquot of 10% (w/v) SiO_2 nanoparticles with a 600 nm photonic bandgap was first dropped onto region C to form a heterostructure for fluorescence enhancement. Then, two types of antibodies were then preloaded in regions C and E to capture the corresponding antigens, i.e., human IgG and AD7c-NTP. After blocking the antibodies, the FITC-labeled antihuman antibody was preloaded in region D and the Cy3-labeled antibodies were preloaded in region B for fluorescent detection at the same concentration, before samples at a series of concentration were dropped onto the inlet. Figure 6c shows the different sample injection modes of the integrated wearable system, which was attached on fingertip and knuckle for body fluid sampling. Furthermore, the fluorescence detection of IgG and AD7c-NTP could be carried out by a simple apparatus for on-site detection. The detection results could also be carried out with a smartphone-based device as our group previously reported,[36] and recorded and transmitted to Adobe Photoshop CS5 to instantly analyze red, green, blue (RGB) data. As depicted in **Figure 7**a,b, the fluorescence intensity of the detection reservoir increased with the concentrations of human IgG and AD7c-NTP from 10 to 500 ng mL^{-1}. The limit of detection defined as three times the standard deviation of the test results for the blank was calculated based on the slope of the calibration

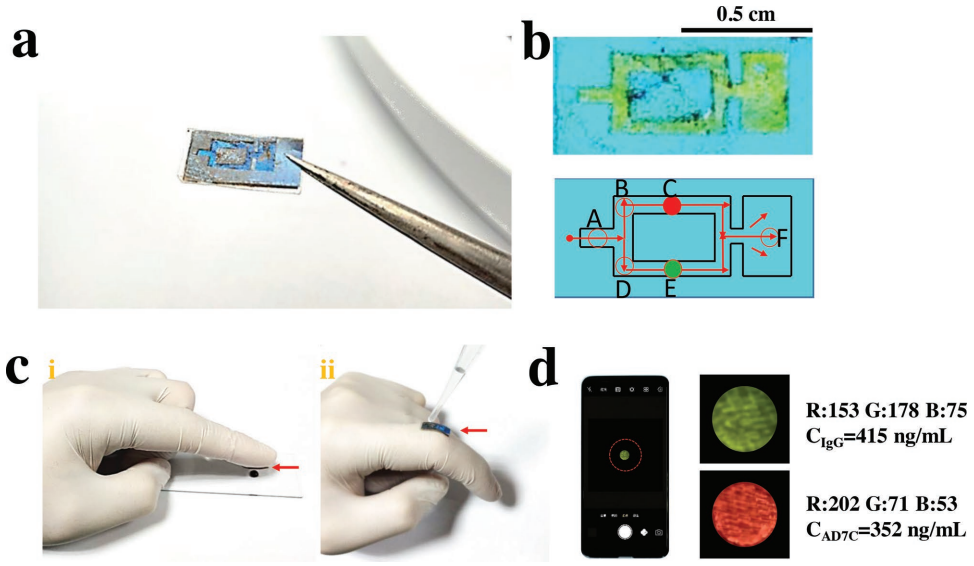

Figure 6. a) Photograph the integrated wearable sensor. b) The optical image and schematic diagram of the microfluidic system of the sensor, A: Inlet for the specimen, B/D: regions preloaded with fluorescence-labeled antibodies (i.e., FITC and Cy3), C/E: detection reservoirs preloaded with the capture antibody, F: waste reservoir. c) Photograph of the integrated wearable system attached on fingertip (i) and knuckle (ii) for body fluid sampling. d) The fluorescence detection of IgG and AD7c-NTP with a smartphone-based device, the detection results were recorded and transmitted to the Adobe Photoshop CS5 to instantly analyze RGB data. (Scale bar: 0.5 cm).

curve, i.e., 12 ng mL^{-1} for human IgG and 4.5 ng mL^{-1} for AD7c-NTP. Similarly, the detection of wrist bending is shown in Figure 7c, as well as the relative changes in resistance with wrist bending at different frequencies, which confirmed the feasibility of using this system for the preliminarily diagnosis of the frequency of static tremors in PD patients.

In this study, we developed a new type of wearable sensor based on the natural ordered structure of the wings of *M. menelaus*. The color and structural properties of the wing were utilized to enhance the fluorescence during the simultaneous analysis of human IgG and AD7c-NTP, where this approach was confirmed as both feasible and effective. The ordered structure was also employed to construct a flexible electronic sensor for obtaining preliminary diagnoses of the frequency of static tremors in PD patients. Thus, wearable sensors that integrate the microfluidic chip and electronic sensor could be effective for the tentative diagnosis of ND. Moreover, the natural ordered structure itself is a promising alternative to POCT and may assist patients in challenging and underdeveloped areas.

Experimental Section

Materials: *M. menelaus* was purchased from Dieyu Company (Shanghai, China). Bovine serum albumin, dopamine hydrochloride and Tris(hydroxymethyl)aminomethane (Tris)-HCl were purchased from Sigma-Aldrich. Monodisperse SiO_2 nanoparticles with diameters of 243, 265, and 331 nm were synthesized using the Stöber–Fink–Bohn method. FITC-labeled human IgG, Cy3-labeled human IgG, goat anti-human IgG, human IgG, FITC-labeled mouse anti-human IgG, rabbit anti-AD7c-NTP, recombinant human AD7c-NTP protein, and Cy3-labeled mouse anti-AD7c-NTP were all purchased from Biosynthesis Biotechnology (Beijing) Co. Ltd. PBS (50×10^{-3} M, pH 7.4) was used for the hybridization of antigen and antibodies. Conductive ink was purchased from Bare Conductive (London) Co. Ltd. Double-sided tape (3 M, VHB 9460) was purchased from 3 M (St. Paul, USA). All of the solutions were prepared with deionized water (18.0 MΩ cm; Milli-Q Gradient System, Millipore) with ultraviolet sterilization. All of the reagents were used as received without further purification.

Experimental Procedures: The process employed for the fabrication of *M. menelaus* wing based wearable sensors is illustrated in Figure 1. First, one posterior wing of *M. menelaus* was selected and the bright blue up layer was separated from the brown under layer. Both of the layers were then treated with a plasma cleaner (DT-01, SZ-Omega Ltd, China) to allow hydrophilic modification for 60 s at 150 W with patterning masks because the wings are hydrophobic. To obtain the microfluidic chip, a patterned wing was utilized directly for the immunoassays, and the patterned under layer was blade-coated with conductive ink (1:10 dilution) to produce the flexible electronic sensor. Finally, the microfluidic chip and flexible electronic sensor were combined for ND diagnosis.

The flow behaviors of solutions on the wing surface were measured. Masks with different sizes and shapes were used to form channels and patterns with plasma treatment. The patterned wings were further soaked and immersed into an aqueous solution of dopamine (2 mg mL^{-1} in 10×10^{-3} M Tris-HCl, pH 8.5) for about 12 h for self-polymerization to obtain the permanent hydrophilicity, and then rinsed with deionized water and dried naturally. Optical images were obtained using a metallographic microscope (HCS302; Olympus), and the reflectance spectra of the treated wings were acquired using an optical-fiber spectrometer (QE 65000; Ocean Optics).

For the screening test, the first step involved determining the optimal experimental conditions. To verify the feasibility of the experiment, 0.2 µL aliquots of PBS (50×10^{-3} M, pH 7.4) containing FITC-labeled human IgG or Cy3-labeled human IgG (100 µg mL^{-1}) were dropped separately onto a glass substrate or the treated wings to observe the effect of fluorescence enhancement. The fluorescence images were obtained using a fluorescence microscope (BX53; Olympus) and the fluorescence spectra of the *M. menelaus* wing, FITC, and Cy3 were acquired with a fluorescence spectrophotometer (F-7000; Hitachi). Next, 0.2 µL aliquots of the three types of 10% (w/v) SiO_2 nanoparticles with diameters of 243, 265, and 331 nm were dropped onto 1 mm dot arrays on the wings. After the assembly of the SiO_2 nanoparticles, 0.2 µL aliquots of Cy3-labeled human IgG (100 µg mL^{-1}) were dropped onto the glass substrate, wing, and SiO_2 dot array to observe the intensity

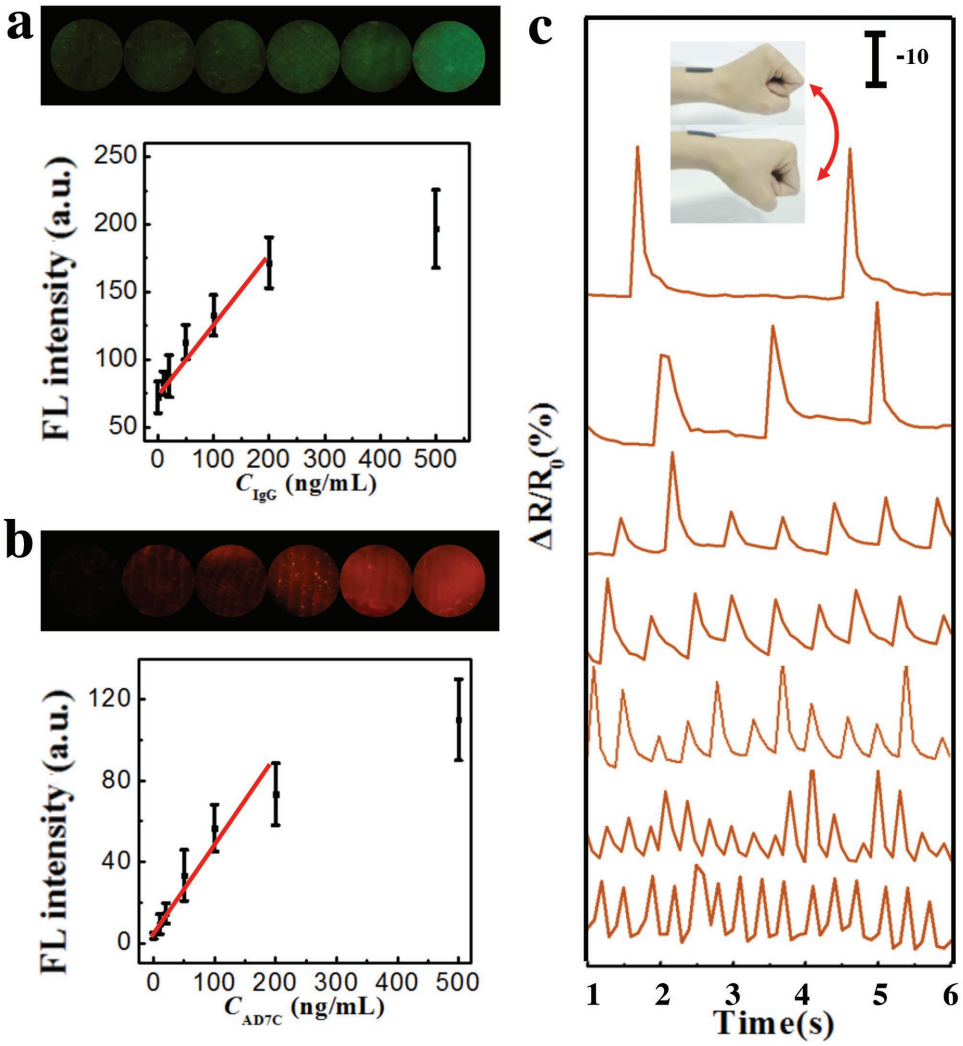

Figure 7. The integrated wearable sensor for physiological and biochemical signal sensing. a) Fluorescence intensity of the detection reservoir (E) in the chip as a function of the human IgG concentration. b) Fluorescence intensity of the detection reservoir (C) in the chip as a function of the AD7c-NTP concentration. c) Relative changes in resistance with wrist bending at different frequencies, where the value of the relative change is 10%.

of the fluorescence signals and determine the optimal size of the SiO_2 nanoparticles. Next, 0.2 µL aliquots of 5%, 10%, and 20% (w/v) SiO_2 nanoparticles with a diameter of 265 nm were dropped onto the dot array to determine the optimal concentration.

For the integrated wearable sensor, the microfluidic chip made by the up layer of *M. menelaus* was combined with the flexible electronic sensor with double-sided tape. The patterned microfluidic chip was fabricated on the wing using plasma with a mask for detecting biomarkers (Figure 6b). The chip had an inlet for the specimen (A), two regions for preloading with fluorescent-labeled antibodies (B/D), two detection zones preloaded with the capture antibody (C/E), and a waste reservoir (F). For the immunoassay, 10% (w/v) SiO_2 nanoparticles with a diameter of 265 nm were dropped onto the detection zone to form a heterostructure for fluorescent enhancement, before a 1.0 µL aliquot of capture antibody (i.e., goat anti-human IgG and rabbit anti-AD7c-NTP) (1 mg mL^{-1}) was dropped onto the detection zone on the chip (to detect IgG and AD7c-NTP). After standing for 1 h at room temperature (25 °C), the detection zone was washed three times with PBS solution (pH = 7.4) to remove any free antibody, before the chip was immersed in PBS solution (pH 7.4) containing 5.0% bovine serum albumin for 1 h to block the remaining active spots. Next, the membrane was washed with PBS solution (pH = 7.4). To detect the antigens, a 1.0 µL aliquot of PBS solution (pH = 7.4) containing 1.0 mg mL^{-1} FITC/Cy3-labeled antibodies was dropped onto the regions for preloading with reagents, before drying completely at room temperature. Then, a concentration gradient series (10–500 ng mL^{-1}) of antigens were dropped onto the inlet to wick through the chip, and the fluorescent images of the detection zones were obtained using a fluorescence microscope (BX53; Olympus) or a smartphone-based device. The images were imported into Adobe Photoshop CS5 to measure the color intensity with RGB data for quantitative detection.

In order to produce the flexible electronic sensor, the under layer of the wing with an ordered structure was utilized to obtain an electrical signal, but it was nonconductive. Hence, conductive ink (1:10 dilution) was blade-coated on the surface after plasma treatment and the electrical characteristics of the electronic sensor were determined with a Keithley 2000 digital multimeter. The relative changes in resistance were measured when the sensor was bent in different directions. In addition, the relative changes in resistance were measured when the finger and wrist of a user bent in different angles, and the mechanical stability test was carried out under >400 cycles with wrist bending at a frequency of 0.2 Hz for 2 000 s.

Statistical Analysis: Experiment results were calculated as means ± SEM and analyzed by Student's *t*-test (Microsoft Excel) for statistical

significance. For each experiment, at least $n = 3$ samples were investigated for fluorescence detection, and error bars indicate the standard deviation of three replicates per data point. Significance level at $p < 0.05$ was considered to be significant.

Supporting Information

Supporting Information is available from the Wiley Online Library or from the author.

Acknowledgements

Z.Z.H. and A.E. contributed equally to this work. This work was supported by the Innovative and Entrepreneurial Talent Recruitment Program of Jiangsu Province, the National Natural Science Foundation of China (Grant Nos. 21405014, 21635001, 21501026, and 51573025), the Key Research and Development Plan of Jiangsu Province BE2016002, the Project of Special Funds of Jiangsu Province for the Transformation of Scientific and Technological Achievements (Grant No. BA2015067), the 111 Project (B17011, Ministry of Education of China), the Natural Science Foundation of Jiangsu Province (Grant Nos. BK20140626 and BK20150024), the Natural Science Foundation of Jiangsu Province (Grant No. BK20140619), and the China Postdoctoral Science Foundation funded project.

Conflict of Interest

The authors declare no conflict of interest.

Keywords

colloidal crystals, electronic, microfluidic, *Morpho menelaus*, neurodegenerative disease

Received: November 9, 2017
Revised: November 29, 2017
Published online:

[1] J. Liu, Y. Zhang, M. Jiang, L. Tian, S. Sun, N. Zhao, F. Zhao, Y. Li, *Biosens. Bioelectron.* **2017**, *91*, 714.
[2] T. Tian, X. Wei, S. Jia, R. Zhang, J. Li, Z. Zhu, H. Zhang, Y. Ma, Z. Lin, C. J. Yang, *Biosens. Bioelectron.* **2016**, *77*, 537.
[3] Y. Fan, J. Liu, Y. Wang, J. Luo, H. Xu, S. Xu, X. Cai, *Biosens. Bioelectron.* **2017**, *95*, 60.
[4] Y. Xie, X. Wei, Q. Yang, Z. Guan, D. Liu, X. Liu, L. Zhou, Z. Zhu, Z. Lin, C. Yang, *Chem. Commun.* **2016**, *52*, 13377.
[5] M. M. Thuo, R. V. Martinez, W. J. Lan, X. Liu, J. Barber, M. B. Atkinson, D. Bandarage, J.-F. Bloch, G. M. Whitesides, *Chem. Mater.* **2014**, *26*, 4230.
[6] B. Gao, H. Liu, Z. Gu, *Anal. Chem.* **2016**, *88*, 5424.
[7] U. G. Wegst, H. Bai, E. Saiz, A. P. Tomsia, R. O. Ritchie, *Nat. Mater.* **2015**, *14*, 23.
[8] B. Yao, J. Chen, L. Huang, Q. Zhou, G. Shi, *Adv. Mater.* **2016**, *28*, 1623.
[9] M. Kuang, J. Wang, L. Jiang, *Chem. Soc. Rev.* **2016**, *45*, 6833.
[10] M. T. Irwin, R. J. Hickey, S. Xie, F. S. Bates, T. P. Lodge, *Macromolecules* **2016**, *49*, 4839.
[11] X. Zhang, T. Wang, C. Jiang, F. Zhang, W. Li, Y. Tang, *Electrochim. Acta* **2016**, *187*, 465.
[12] M. Cheng, Y. Wang, L. Yu, H. Su, W. Han, Z. Lin, J. Li, H. Hao, C. Tong, X. Li, F. Shi, *Adv. Funct. Mater.* **2015**, *25*, 6851.
[13] H. Butt, A. K. Yetisen, D. Mistry, S. A. Khan, M. U. Hassan, S. H. Yun, *Adv. Opt. Mater.* **2016**, *4*, 497.
[14] Z. Han, Z. Mu, B. Li, Z. Wang, J. Zhang, S. Niu, L. Ren, *ACS Nano* **2016**, *10*, 8591.
[15] N. N. Lal, K. N. Le, A. F. Thomson, M. Brauers, T. P. White, K. R. Catchpole, *ACS Photonics* **2017**, *4*, 741.
[16] Q. Li, Q. Zeng, L. Shi, X. Zhang, K.-Q. Zhang, *J. Mater. Chem. C* **2016**, *4*, 1752.
[17] Z. Mu, H. Gu, B. Zhang, J. Zheng, Z. Zhai, X. He, Y. Zhao, *J. Mater. Chem. C* **2017**, *5*, 9540.
[18] A. H. V. Schapira, C. W. Olanow, J. T. Greenamyre, E. Bezard, *Lancet* **2014**, *384*, 545.
[19] K. R. Brunden, V. M. Lee, A. B. Smith III, J. Q. Trojanowski, C. Ballatore, *Neurobiol. Dis.* **2017**, *105*, 328.
[20] V. Khurana, J. Peng, C. Y. Chung, P. K. Auluck, S. Fanning, D. F. Tardiff, T. Bartels, M. Koeva, S. W. Eichhorn, H. Benyamini, *Cell Syst.* **2017**, *4*, 157.
[21] L. Scott, V. L. Dawson, T. M. Dawson, *Exp. Nephrol.* **2017**, *298*, 191.
[22] M.-T. Heemels, *Nature* **2016**, *539*, 179.
[23] M. S. Xydakis, L. Belluscio, *Lancet Neurol.* **2017**, *16*, 415.
[24] A. D. Gitler, P. Dhillon, J. Shorter, *Dis. Models & Mech.* **2017**, *10*, 499.
[25] B. Dubois, H. Hampel, H. H. Feldman, P. Scheltens, P. Aisen, S. Andrieu, H. Bakardjian, H. Benali, L. Bertram, K. Blennow, *Alzheimers Dement.* **2016**, *12*, 292.
[26] D. W. Dickson, *Acta Neuropathol.* **2005**, *109*, 14.
[27] G. B. Frisoni, M. Boccardi, F. Barkhof, K. Blennow, S. Cappa, K. Chiotis, J.-F. Démonet, V. Garibotto, P. Giannakopoulos, A. Gietl, *Lancet Neurol.* **2017**, *16*, 661.
[28] M. Synofzik, T. Gasser, *Mov. Disord. Clin. Pract.* **2017**, *4*, 8.
[29] P. J. Kahle, M. Jakowec, S. J. Teipel, H. Hampel, G. M. Petzinger, D. A. Di Monte, G. D. Silverberg, H. J. Möller, J. A. Yesavage, J. R. Tinklenberg, E. M. Shooter, G. M. Murphy, *Neurology* **2000**, *54*,1498.
[30] P. Averback, *Neurology* **2000**, *55*, 1068.
[31] J. Benito-León, A. Domingo-Santos, A. Hassan, J. E. Ahlskog, J. Y. Matsumoto, J. H. Bower, *Neurology* **2016**, *87*, 341.
[32] Y. Zhang, L. Mu, R. Zhou, P. Li, J. Liu, L. Gao, L. Heng, L. Jiang, *J. Mater. Chem. C* **2016**, *4*, 9841.
[33] S. H. Kim, K.-S. Kim, K. Char, S. I. Yoo, B.-H. Sohn, *Nanoscale* **2016**, *8*, 10823.
[34] B. Gao, L. Tang, D. Zhang, Z. Xie, E. Su, H. Liu, Z. Gu, *ACS Appl. Mater. Interfaces* **2017**, *9*, 32577.
[35] E. Eftekhari, W. Wang, X. Li, A. Nikhil, Z. Wu, R. Klein, I. S. Cole, Q. Li, *Sens. Actuators, B* **2017**, *240*, 204.
[36] J. Chi, B. Gao, S. Mi, F. Zhang, E. Su, L. Hong, Z. Gu, *Anal. Chem.* **2017**, *89*, 7727.